HHS Public Access

Author manuscript

J Control Release. Author manuscript; available in PMC 2020 September 10.

Published in final edited form as:

J Control Release. 2019 September 10; 309: 1–10. doi:10.1016/j.jconrel.2019.07.024.

Ultrasound/microbubble-mediated targeted delivery of anticancer microRNA-loaded nanoparticles to deep tissues in pigs

Tommaso Di Ianni[1,**], **Rajendran J.C. Bose**[1], **Uday K. Sukumar**[1], **Sunitha Bachawal**[1], **Huaijun Wang**[1], **Arsenii Telichko**[1], **Carl Herickhoff**[1], **Elise Robinson**[1], **Sam Baker**[2], **José G. Vilches-Moure**[2], **Stephen A. Felt**[2], **Sanjiv S. Gambhir**[1,3], **Ramasamy Paulmurugan**[1,**], **Jeremy D. Dahl**[1]

[1]Department of Radiology, School of Medicine, Stanford University, Stanford, California

[2]Department of Comparative Medicine, School of Medicine, Stanford University, Stanford, California

[3]Department of Bioengineering, Department of Materials Science and Engineering, Stanford University, Stanford, California

Abstract

In this study, we designed and validated a platform for ultrasound and microbubble-mediated delivery of FDA-approved pegylated poly lactic-co-glycolic acid (PLGA) nanoparticles loaded with anticancer microRNAs (miRNAs) to deep tissues in a pig model. Small RNAs have been shown to reprogram tumor cells and sensitize them to clinically used chemotherapy. To overcome their short intravascular circulation half-life and achieve controlled and sustained release into tumor cells, anticancer miRNAs need to be encapsulated into nanocarriers. Focused ultrasound combined with gas-filled microbubbles provides a noninvasive way to improve the permeability of tumor vasculature and increase the delivery efficiency of drug-loaded particles. A single handheld, curvilinear ultrasound array was used in this study for image-guided therapy with clinical-grade SonoVue contrast agent. First, we validated the platform on phantoms to optimize the microbubble cavitation dose based on acoustic parameters, including peak negative pressure, pulse length, and pulse repetition frequency. We then tested the system *in vivo* by delivering PLGA nanoparticles co-loaded with antisense-miRNA-21 and antisense-miRNA-10b to pig liver and kidney. Enhanced miRNA delivery was observed (1.9- to 3.7-fold increase) as a result of the ultrasound treatment compared to untreated control regions. Additionally, we used highly fluorescent semiconducting polymer nanoparticles to visually assess nanoparticle extravasation. Fluorescent microscopy suggested the presence of nanoparticles in the extravascular compartment. Hematoxylin and eosin staining of treated tissues did not reveal tissue damage. The results presented in this manuscript

**Corresponding author.

Declaration of Interest

None.

suggest that the proposed platform may be used to safely and noninvasively enhance the delivery of miRNA-loaded nanoparticles to target regions in deep organs in large animal models.

Keywords

Ultrasound; microbubbles; nanoparticles; microRNAs; cancer treatment; targeted drug delivery

Introduction

MicroRNAs (miRNAs) are small, non-coding regulatory molecules responsible for mediating several signaling pathways that are crucial for cancer initiation and progression, invasion and metastasis, and drug resistance [1]. Abnormal miRNA regulation caused by genetic or epigenetic mechanisms may result in oncogenic effects [2]. Counterbalancing the function of up- or downregulated miRNAs via exogenous manipulation with synthetic sense-miRNA or antisense-miRNA (AmiRNA or AmiR), has shown anticancer treatment effects *in vitro* and *in vivo* [3], [4].

A major challenge of using RNA interference for cancer therapy is the low circulation half-life of naked synthetic small RNAs when they are injected into the bloodstream, which is due to abundant nucleases [5], [6]. A viable strategy to circumvent the rapid intravascular degradation is to shield the miRNAs by enclosing them into nanocarriers [3]. Encapsulation of therapeutic agents into nanoparticles (NPs), including liposomes and polymer or albumin-based NPs, has been extensively investigated in cancer treatment [7]. Importantly, NPs may be designed to enhance the drug biodistribution, accumulation kinetics, and sustained release profile by taking advantage of the tumor enhanced permeability and retention (EPR) effect, i.e. the abnormal permeability of the cancer vas culature that allows larger NPs, which are normally prevented from extravasating, to reach the cancer tissue. This targeted delivery mechanism is particularly interesting as it offers the possibility to increase the therapeutic efficacy of intravenously administered anticancer formulations while minimizing adverse effects in healthy organs due to unintended drug accumulation [8]. Nevertheless, EPR effect-based targeting is highly sensitive to pathophysiological factors like abnormal tumor vascular morphology, variable blood flow rate, and high interstitial fluid pressure, leading to low delivery efficiency and highly heterogeneous drug distribution [9].

Focused ultrasound (US) combined with gas-filled microbubbles (MBs) provides a noninvasive way to enhance the delivery of large-sized particles or molecules by increasing the tumor vascular permeability through a process named sonoporation [10], [11]. Depending on the acoustic pressure and frequency of the US field, the energy deposited within the US focus generates stable MB oscillations or may create violent MB collapse. The two phenomena are referred to as non-inertial and inertial cavitation, respectively. MB cavitation promotes the formation of fluid microjets, shockwaves, streaming, and cavitation forces, which in turn may breach the vessel walls facilitating NP extravasation and increasing vascular porosity. Additionally, focused US enables targeted and controlled drug delivery with high spatial selectivity, as the US-induced effects are spatially limited to the US focus, which can be directed to any desired target region. Previous studies have

demonstrated that this approach is effective to normalize the high variability of the EPR effect for the treatment of hepatocellular carcinoma [4], colon cancer [12], pancreatic cancer [13], [14], and breast cancer metastasis in the brain [15] in a preclinical setting. Clinically, US and MB therapy has been used for the treatment of unresectable pancreatic cancer [16] and Alzheimer's disease [17].

Alternative US-mediated drug delivery systems rely on the use of US-sensitive MBs or liposomes as drug carriers and consequent drug release *in situ* through MB destruction or particle activation (e.g., via thermal triggering). This method has been previously tested in a number of preclinical applications in large animal models. Dewitte et al. delivered messenger RNA to lymph nodes in dogs through destruction of drug-loaded MBs [18]. Similarly, Liu et al. used MBs loaded with miR-21 as delivery vectors for cardiac gene transfection in pigs [19]. Importantly, US combined with drug-loaded MBs/liposomes was recently used in clinical trials to investigate its feasibility in the treatment of pancreatic and liver cancer patients [16], [20]. Although effective in targeted delivery, these approaches are not able to achieve a controlled and sustained release, as the free drug diffuses in the blood stream to reach the target tissue once it is released from the carriers, and this may be a limiting factor in the case of drugs with short circulation half-lives.

A system for image-guided US and MB-mediated targeted delivery of miRNA-loaded NPs was implemented and tested in mice by Wang et al. [12] and subsequently used in a longitudinal study investigating the effect of two complementary miRNAs (miR-122 and AmiR-21) combined with doxorubicin in drug-resistant hepatocellular carcinoma [21]. miRNAs were loaded into NPs made of FDA-approved, biodegradable, and biocompatible pegylated poly lactic-co-glycolic acid (PLGA-PEG) polymer [22]. US-induced inertial cavitation of circulating MBs was shown to significantly increase the amount of delivered miRNAs and to decrease the tumor growth after repeated cycles of combined therapy [21].

The objective of the current study was to design and validate a platform for targeted delivery of miRNA-loaded NPs to deep tissues in large animal models, as a further step toward clinical translation. We used PLGA-PEG NPs co-loaded with AmiR-21 and AmiR-10b, two antisense miRNAs antagonizing the function of endogenous miR-21 and miR-10b, respectively. These miRNAs have been reported to be significantly upregulated in a number of malignancies and to play a role in preventing apoptosis and promoting tumor migration and metastatic spread [1], [23]. Silencing the expression of miR-21 and miR-10b through administration of antagonizing miRNAs was shown to elicit substantial reduction of tumor growth [3]. A single diagnostic US transducer array was used for image-guidance and therapy in combination with clinical-grade SonoVue contrast agent (Bracco Imaging S.p.A., Milan, Italy). The system was first tested on phantoms to optimize relevant acoustic parameters for maximizing inertial cavitation dose. miRNA-loaded PLGA-PEG NPs were administered systemically in combination with highly fluorescent semiconducting polymer nanoparticles (SPNs), and US treatment was delivered to the liver and kidney of healthy pig models to validate the feasibility of the setup *in vivo*. Uptake of PLGA-PEG NPs was assessed by quantifying the levels of delivered therapeutic miRNAs by quantitative reverse transcription polymerase chain reaction (qRT-PCR), and immunofluorescence (IF)

microscopy of SPNs was performed to confirm the presence of fluorescent NPs into the parenchyma.

Materials and methods

Delivery platform and ultrasound system

The implemented platform for targeted delivery of miRNA-loaded NPs to deep tissues in large animal models is schematically depicted in Figure 1A. MBs and NPs are co-administered intravenously, and MB cavitation induced by the focused US beam increases the vascular permeability in the targeted region and facilitates transport of NPs out of the vascular compartment, where the miRNA cargo is released in the parenchyma.

A single handheld, curvilinear array transducer (C5-2v; Verasonics Inc., Redmond, WA, USA) was used with a Vantage 256 research scanner (Verasonics Inc.) for image-guided therapy. During the animal experiments, the probe was housed in a custom 3-D printed holder and mounted on a jointed flex-arm stand (Dino-Lite MS-52B; AnMo Electronics Corp., Taipei, Taiwan). The positioning system enables comfortable freehand scanning and allows for probe fixation in the desired target location by locking the arm joints. The custom holder allows for rotation of the probe in the elevation direction at angular increments of 2.5° (Figure 1B).

A B-mode imaging sequence consisting of 13 unfocused emissions steered between ± 9° with a center frequency of 4 MHz was used for image guidance (Figure 1C) [24], [25]. The beamformed images were displayed with a dynamic range of 60 dB and a frame rate of 6 frames/s. The mechanical index (MI) of the B-mode emissions was 0.15 to avoid nonspecific destruction of bubbles from the imaging pulses.

Therapy was delivered using a focused beam with an F-number of 1.2 and a center frequency of 2 MHz. The emitted acoustic pressure was measured in the XZ and YZ planes with a focus at 70 mm using a needle hydrophone (HNC-0500; Onda, Sunnyvale, CA, USA) in degassed water (Figure 1D). The full width at half maximum was 1.9, 2.9, and 21.8 mm in the X, Y, and Z directions, respectively. For calibration, the peak negative pressure was measured with increasing excitation voltage and derated with an attenuation factor of 0.5 dB/(cm MHz).

Microbubbles

Clinically approved SonoVue contrast agent (approved in the United States under the name Lumason) was used for all the phantom and animal experiments. The agent consists of MBs made of a stabilized sulfur hexafluoride gas core surrounded by a phospholipid monolayer shell, with a mean diameter range of 1.5 to 2.5 μm [26]. The contrast agent was resuspended in sterile 0.9% physiological saline and diluted to obtain the desired concentration.

Phantom experiments

A phantom study was performed to determine the effects of acoustic parameters on the MB cavitation. A concentration of approximately 10^7 MB/ml was used. The solution was circulated in a 4-mm diameter flow channel embedded in tissue-mimicking material (Model

527; ATS, Bridgeport, CT, USA) using a flow pump (ISM596D; IDEX, Oakharbor, WA, USA). A mean velocity of 1.2 mm/s was maintained. The phantom setup is depicted in Figure 2A. The US probe was positioned at a distance of 70 mm from the vessel, and a focused US beam was used to induce MB cavitation. Peak negative pressure, pulse length, and pulse repetition frequency (PRF) of the therapy pulse were varied as reported in Figure 2B. Two hundred pulses were delivered for each set of acoustic parameters.

To measure the inertial cavitation dose (ICD), the broadband emission generated by inertial cavitation events was detected by using the same transducer array. The root mean square (RMS) intensity of the recorded echoes was calculated (over the frequency range 5.5 MHz ± 150 kHz) and integrated over the number of delivered pulses. The measurement was first performed on a saline-filled vessel to estimate the baseline noise floor, and then repeated with circulating MBs. The baseline noise floor was then subtracted from the RMS intensity resulting from MB cavitation to obtain the ICD [27]. We did not expect the occurrence of cavitation events in the absence of MBs in any of the tested conditions, as the pressures used are below the statistical threshold for water [28]. The data processing and ICD calculation were performed in MATLAB (The MathWorks, Inc., Natick, MA, USA).

Analysis of variance (ANOVA) was used to assess the presence of a significant effect of each parameter on the measured ICD. A Wilcoxon signed-rank test was used for pairwise comparisons within each set of acoustic parameters. All statistical tests were performed in RStudio 1.1.442, and statistical significance was considered for $p < 0.05$.

Nanoparticle synthesis

Pegylated PLGA nanoparticles loaded with AmiRNA-21 and AmiRNA-10b— PLGA-PEG NPs loaded with AmiR-21 and AmiR-10b were prepared using a double emulsion solvent evaporation technique as described previously [3], [12]. In brief, the miRNAs (10 nmol) were complexed with spermidine in an N/P ratio of 15:1 in DNAse/RNAase free water for 15 min at room temperature. The miRNA-spermidine complex was added dropwise to the stirred solution of PLGA-PEG polymer (10 mg) dissolved in dichloromethane (1 ml) containing 3% Span-80. Successively, the complex was sonicated for 60 sec at 40% amplitude (SFX-150; Branson Ultrasonics, Danbury, CT, USA) in an ice bath to form the first emulsion. The mixture was added to 5 ml of emulsifying water (Tween-80, 1% w/v) and sonicated at 40% amplitude in an ice bath for 60 sec to form the second emulsion, followed by stirring for 3 h to facilitate evaporation of the dichloromethane. The NPs were then sterile filtered using a 0.45-μm syringe filter (Whatman PURADISC 25 AS; GE Healthcare Life Sciences, Pittsburg, PA, USA). Excess surfactants and free miRNAs were removed by centrifuging the NPs three times in sterile DNAse/RNAase free water (Invitrogen, Grand Island, NY, USA) at 3000 rpm using an ultracentrifuge filter device with 100 kDa MWCO Membrane (Amicon Ultra; Merk Millipore, Burlington, MA, USA). The size and zeta-potential of the PLGA-PEG NPs were measured using a Zetasizer Nano ZS90 (Malvern Panalytical Ltd., Malvern, U.K.) dynamic light scattering (DLS) system. NP concentration was quantified with nanoparticle tracking analysis (NTA) by NanoSight NS300 (Malvern) using 10 mg of PLGA-PEG dissolved in 3.3 ml of deionized water. Gel electrophoresis was used to determine encapsulation and loading

efficiency of miRNAs after extracting the loaded miRNAs from a fixed amount of NP solution as well as from the washed solution.

Semiconducting polymer nanoparticles—SPNs are fluorescent NPs made of organic and biocompatible polymer material with high brightness and controllable dimensions. We synthesized these particles with characteristics similar to the PLGA-PEG NPs (see nanoparticles characterization result section). Owing to their strong fluorescence in the far-red region, even after tissue fixation in 4% paraformaldehyde, SPNs were an ideal proxy to confirm NP extravasation via IF confocal microscopy. SPNs were prepared following a protocol described previously [29] with minor modifications. Briefly, 15 mg of 1,2-Distearoyl-sn-glycero-3-phosphoethanolamine-N-[methoxy(polyethyleneglycol)-2000] (ammonium salt; DSPE-mPEG) were dissolved into 1 ml of dichloromethane solution containing 0.25 mg/ml of poly[2,7-(9,9-dioctylfluorene)-alt-4,7-bis(thiophen-2-yl)benzothiadiazole] (PFODBT). The mixture was poured into distilled-deionized water (10 mL) under continuous sonication with an ultrasonic sonifier (Branson Ultrasonics) at a power output of 6 W RMS for 10 min on ice. Dichloromethane was evaporated at 45°C under nitrogen atmosphere. Finally, the aqueous solution of SPNs was filtered through a 0.22 μm polyvinylidene fluoride membrane filter. The size and zeta-potential of the SNPs were measured by DLS, and NP concentration was quantified by NTA.

Animal preparation

The experimental protocol for the animal study was approved by the Institutional Animal Care and Use Committee at Stanford University. The university's animal care and use program and facilities are AAALAC International accredited, PHS-assured, and USDA licensed. Healthy female Yorkshire pigs (Pork Power Farms, Turlock, CA; weight range: 28-32 kg; age range: 11-13 weeks) were used in this study. The animals were fed a commercially prepared balanced ration ad libitum (Nature's Match Sow & Pig Complete, Purina Mills LLC, St Louis, MO) and fasted overnight prior to the compound administration and imaging procedure. Reverse-osmosis water delivered through both an automatic watering system and in a bowl was made available at all times.

The animals were anesthetized with intramuscularly administered tiletamine HCL and zolazepam HCL (8 mg/kg; Telazol; Pfizer, New York, NY, USA), intubated, and kept under inhalant 2-4% isoflurane in oxygen (2 l/min). Vascular access was created via an intravenous catheter inserted in the marginal ear vein. Pigs were administered acetylsalicylic acid (Aspirin; Wedgewood, Swedesboro, NJ, USA) intravenously (3.5 mg/kg) 5 min prior to NP injection. Vital signs including heart rate, respiratory rate, blood pressure, oxygen saturation, end-tidal CO_2 pressure, EKG, and body temperature were monitored during the entire procedure with an anesthesia and monitoring system (SurgiVet, Dublin, OH, USA).

Drug delivery protocol

Prior to the therapy procedure, the liver and right kidney were imaged from a subcostal view. Easily-accessible regions were identified in the two organs at a depth of approximately 70 mm, and the two imaging windows were marked on the skin. A solution of PLGA-PEG NPs co-loaded with AmiR-21 and AmiR-10b (8 ml; 8×10^{11} NP/ml) and SPNs (3 ml; 5.13 ×

10^{13} NP/ml) was administered with a bolus injection. A volume of 25 ml SonoVue was diluted with sterile 0.9% physiological saline in a 40-ml solution. The MB solution was continuously infused at a rate of 16.67 μl/s using a syringe pump (Medfusion 3500; Smiths Medical, Dublin, OH, USA) for the entire duration of the therapy procedure (approximately 40 min). The dose of SonoVue was higher than the maximum dose of 2.4 + 2.4 ml (bolus + bolus) recommended for ultrasonography of the liver [26]. However, we infused the solution over an extended period of time, and the increased dose was partly compensated for by MB clearance.

Focused US treatment was initiated 2 min after the MB infusion was started to ensure a steady state of MB perfusion. The treatment was performed first in the liver and subsequently in the right kidney in a region adjacent to the lower pole. A 10-cycle focused US pulse was used for drug delivery with a derated in-situ peak negative pressure of 5.3 MPa (MI = 3.8; I_{spta} = 26.4 mW/cm^2), based on the optimized system parameters from the phantom experiments. Eleven therapy foci were used in each plane, with a lateral displacement equal to the measured lateral FWHM (Figure 1C). The probe was rotated over 10 angular positions to cover a therapy volume of approximately 20 × 20 × 27.5 mm^3. For each therapy region, eight hundred pulses were delivered with a PRF of 4 Hz.

In vivo experiments and tissue collection

We preliminarily tested the US platform in two animals (Pig 1 and 2; data not shown) to verify US imaging parameters, test probe positioning to target liver and kidney, and determine possible toxic reactions to the co-administration of PLGA-PEG NPs and SPNs with simultaneous infusion of MBs. It was not possible to analyze tissues from these animals due to the inability to identify the therapy regions at necropsy, as discussed below.

A third animal (Pig 3) was anesthetized, administered an injection of miRNA-loaded PLGA-PEG NPs, and recovered following anesthesia. This pig was re-anesthetized 24 h later and euthanized by means of injection of pentobarbital sodium (Beuthanasia-D; Schering-Plough Animal Health, Union, NJ, USA). Tissue was collected from the liver, lung, heart, spleen, and pancreas for miRNA quantification to evaluate the drug biodistribution 24 h post NP injection.

A fourth animal (Pig 4) received NP administration followed by US treatment with MB infusion. An US-guided injection of 300 μl Matrigel (BD Matrigel Matrix Phenol Red-Free; BD Biosciences, San José, CA, USA) mixed with indocyanine green (ICG; Intrace Medical SA, Lausanne, Switzerland) dye was performed adjacent to the area targeted with the US to facilitate its localization *ex vivo* by optical imaging. The animal was kept under anesthesia until euthanasia 4 h post NP injection. The whole liver was resected and imaged with an IVIS Spectrum scanner (PerkinElmer, Chicago, IL, USA) to locate the targeted area marked by the Matrigel-embedded ICG dye, and samples were collected from the treated volume and from an untreated region in a distal end of the organ for control. Tissue samples were collected from the right kidney in the treated region (lower pole) and from the left untreated kidney for control. These samples were used for miRNA quantification, IF analysis, and histological analysis. In addition, samples of lung, heart, spleen, and pancreas were

harvested for miRNA quantification to evaluate the drug biodistribution 4 h post NP injection.

A liver tissue sample was obtained from a fifth animal (Pig 5) that did not receive any injection or US treatment. This sample was used for a baseline quantification of endogenous miRNA (miR-122) and considered as a negative control.

MicroRNA quantification

Harvested samples for miRNA quantification from Pig 3 and Pig 4 were snap-frozen on dry ice immediately after resection. The levels of delivered therapeutic AmiR-21 and AmiR-10b were evaluated by using qRT-PCR. Samples of tissue of 100 mg were homogenized using a PRO250 tissue homogenizer (PRO Scientific, Oxford, CT, USA) in 300 μl lysis buffer for 3 min. Total RNA (messenger RNA and miRNA) was isolated from the lysates using mirVana miRNA Isolation Kit (Life Technologies, Grand Island, NY, USA) adopting the total RNA extraction procedure according to the manufacturer's protocol.

For miRNA quantification, 50 ng of total RNA was reverse transcribed using RT-primers (Life Technologies) for AmiR-21 and AmiR-10b using a custom ordered TaqMan kit and a microRNA Reverse Transcription Kit (Life Technologies). qRT-PCR was performed using cDNA (5 ng equivalent of total RNA) combined with TaqMan RT-PCR reagents (primer and probe mix) of AmiR-21 and AmiR-10b. qRT-PCR was performed by 2 min incubation at 50 °C followed by activation of the DNA polymerase at 95 °C for 10 min, 60 cycles of 95 °C for 15 sec, and 60 °C for 60 sec in a Bio-Rad CFX96 Touch™ Real-Time PCR Detection System (Bio-Rad, Hercules, CA). The level of AmiR-21 and AmiR-10b was calculated using the $2^{-\Delta CT}$ method [30]. The qRT-PCR quantification was repeated three times for each analyzed sample. The miRNA levels were normalized to the endogenous level of miR-122 in Pig 5, which was administered neither NPs nor US and MB therapy and served as a control.

Immunofluorescence staining

Tissue samples for IF analysis from Pig 4 were fixed in 4% paraformaldehyde overnight at 4 °C, immersed in a 30% sucrose solution for cryoprotection, and frozen at −80 °C. Tissues were then embedded in optimal cutting temperature media (Fisher Scientific, Whitby, Ontario, Canada) and cryosectioned in slices of 10 μm thickness. The sections were stained for F-actin (using phalloidin) and vascular endothelial cell marker CD-31 for visualizing the cytoskeleton and blood vessels, respectively.

The slices were rinsed in phosphate-buffered saline for 10 min, permeabilized in 0.5% Triton-X 100 in saline, and incubated in a blocking solution of 3% bovine serum albumin (Sigma, St. Louis, MO, USA), 3% normal goat serum (Sigma), and 3% normal donkey serum (Sigma) for 60 min at room temperature. The samples were then incubated with a rabbit-anti-human CD31 primary antibody (1:100; Abcam, Cambridge, MA, USA) at 4 °C overnight in a humidifying chamber. Samples were then incubated with a goat anti-rabbit Alexa Fluor 488 IgG secondary antibody (1:250; Invitrogen) and Alexa Fluor 633-phalloidin (1:100; Invitrogen) for 30 min. Samples were mounted in aqueous mounting media (BiogeneX, San Ramon, CA, USA) and imaged with a LSM710 metaconfocal microscope (Carl Zeiss GmbH, Jena, Germany) at 20X magnification. A tiled confocal micrograph was

obtained using a motorized staged controlled by the microscope acquisition software (AxioVision; Carl Zeiss). Image analysis was performed in Fiji 2.0.0 [31].

Hematoxylin and eosin staining

Kidney and liver samples from Pig 4 were fixed in 10% neutral buffered formalin at room temperature, routinely processed, embedded in paraffin, and sectioned with a microtome into 5 μm thick slices for routine hematoxylin and eosin (H&E) staining. Tissue assessment was performed blindly by a veterinary pathologist.

Results

Inertial cavitation dose measurement in phantom

The results of the ICD measurements in phantom with varying acoustic parameters are reported in Figure 2C, 2D, and 2E. In each plot, the ICD was normalized to the mean ICD for the lowest value of each parameter, i.e. peak negative pressure of 0.13 MPa, pulse length of 2 cycles, and PRF of 1 Hz.

The ICD was significantly influenced by all the parameters tested (ANOVA; $p < 0.0001$). Peak negative pressure and pulse length had the highest effect on cavitation, with a 33- and 38-fold maximum increase for the pressure and pulse length, respectively. A plateau was reached for pressure above 2.57 MPa (Figure 2C), and no statistical difference was found between 2.57, 3.85, and 5.34 MPa ($p = 0.89$ for 2.57 and 3.85; $p = 0.71$ for 2.57 and 5.34; $n = 4$). Similarly, there was no statistical significance between pulse lengths of 5, 10, and 20 cycles (Figure 2D; $p = 0.312$ for 5 and 10; $p = 0.061$ for 5 and 20; $n = 4$). Conversely, the PRF caused a decreasing trend on the measured ICD, although the difference was minimal (< 2-fold maximum decrease). No statistical significance was found between 4, 10, and 20 Hz (Figure 2E; $p = 0.216$ for 4 and 10; $p = 0.112$ for 4 and 20; $n = 4$).

Nanoparticle characterization

Pegylated PLGA nanoparticles loaded with AmiRNA-21 and AmiRNA-10b— Particle characterization results are reported in Figure 3. The average size and zeta-potential of PLGA-PEG NPs measured by DLS were 115.3 ± 18 nm (mean ± SD; polydispersity index (PDI) <0.25; Figure 3C) and −32.2 ± 2.8 mV (mean ± SD; Figure 3D), respectively. The particle concentration quantified by NTA was 3.3×10^{12} NP/ml (Figure 3B). The miRNA encapsulation efficiency was analyzed using organic/aqueous extraction method and was equal to 60.1 ± 5.3%. Size and shape of PLGA-PEG NPs were further confirmed by transmission electron microscopy with phosphotungstic acid as negative staining (data not shown). The loading efficiency of antisense-miRNAs was quantified by optical CCD camera imaging of PLGA-PEG NPs loaded with Cy5-AmiR-21 after resolving the NPs by agarose gel electrophoresis. The average number of antisense-miRNAs encapsulated in various NP formulations was estimated to be in the range of 600 to 1000 molecules/NP. The results indicate that co-loading of AmiR-21 and AmiR-10b in PLGA-PEG NPs is found almost at equimolar concentration in NPs prepared in different batches. The antisense-miRNAs extracted from the equimolar mixture of NPs formulated with each antisense-miRNAs (AmiR-21 and AmiR-10b) separately was used as control.

Semiconducting polymer nanoparticles—The average size and zeta-potential of SPNs measured by DLS were 116 ± 5 nm (mean ± SD; PDI = 0.17; Figure 3C) and −30 ± 3 mV (mean ± SD; Figure 3D), respectively. The data reveal that the presence of DSPE-mPEG slightly affects the size of SPNs but increases their zeta potential, possibly yielding improved aqueous stability. It can be noted that the measured size and zeta-potential of SPNs were similar to those of miRNA-loaded PLGA-PEG particles. Therefore, we expect a correlation between the amount of extravasated SPNs and PLGA-PEG NPs, as we found in previous studies in small animals [12]. For this reason, in this study we used SPNs as a model drug to confirm NP extravasation.

To test the *in vitro* cell-labelling efficiency of SPNs, breast cancer cell lines (SKBR3 and MDA-MB-231) were used as a model. After incubation of cells with SPNs at a concentration of 50 μg/ml at 37 °C for 8 h, live cells were imaged by fluorescence microscopy (Figure 3E). The excitation/emission wavelength was 523/630 nm. Bright fluorescence of SPN clusters increased significantly in cells transfected with SPNs.

Delivery of PLGA nanoparticles loaded with AmiRNA-21 and AmiRNA-10b

qRT-PCR quantification of exogenous AmiR-21 and AmiR-10b delivered to liver and kidney in Pig 4 is reported in Figure 4A and 4B. The miRNA levels were normalized to the level of endogenous miR-122 in the liver of a negative control animal that received neither NP injection nor US treatment (Pig 5). The levels of AmiR-21 in the liver (Figure 4A) increased 991-fold in response to PLGA-PEG NP injection alone (untreated region) and 1884-fold after US and MB therapy (treated region), compared to the control animal. The level of AmiR-10b in the liver increased 89-fold due to NP injection and 245-fold post US treatment compared to the control animal. Therefore, US and MB-mediated delivery yielded a 1.9- and 2.7-fold increase of the two exogenous miRNAs in liver. Levels of AmiR-21 quantified in the kidney (Figure 4B) increased 160-fold due to NP injection and 598-fold in response to US treatment, while the levels of AmiR-10b increased 15- and 42-fold for the two cases. Hence, the increase due to US and MB treatment was 3.7- and 2.8-fold for the two exogenous miRNAs in the kidney.

The biodistribution of AmiR-21 at 4 h (Pig 4) and 24 h (Pig 3) is reported in Figure 4C (log scale). The plots show an overall decrease of exogenous miRNA in the liver, kidney, and heart at 24 h compared to the 4 h time point. In contrast, the level of delivered AmiR-21 increased substantially at 24 h in the lung and spleen (36- and 6-fold, respectively).

Immunofluorescence analysis

To confirm that increased level of exogenous miRNA was due to enhanced delivery of PLGA-PEG NPs in response to the US and MB-mediated therapy, we performed IF confocal microscopy of SPNs as a model system to mimic the miRNA-loaded PLGA-PEG NPs. Representative IF images are shown in Figure 5 for both a treated (Figure 5A and B) and untreated (Figure 5C) liver region in Pig 4. The IF images confirmed presence of SPNs in the liver parenchyma and in regions not co-located with blood vessel marker CD-31, supporting the hypothesis of NP extravasation. Increased presence of SPNs was also noticed in the treated liver samples with respect to the untreated region, although we did not perform

a quantitative assessment of the fluorescence levels due to the unequal distribution of the IF signal in various tissue region. It is important to point out that the total amount of administered SPNs was ~24x higher than the number of PLGA-PEG NPs.

Histological analysis

Representative H&E-stained sections of pig liver and kidney tissues from Pig 4 are shown in Figure 6 for the treated and untreated regions. The stained samples were examined to detect changes such as hemorrhage, inflammation, and edema.

The liver and kidney samples that received US-MB treatment had no evidence of hemorrhage, inflammation, or edema attributable to the experimental treatment. Mild s inusoidal distention was observed in numerous lobules in both treated and untreated liver samples. The condition was globally present throughout the liver and was deemed to result from a preexisting condition, and not due to the US-MB treatment. Overall, the US-MB treatment did not cause tissue damage in the liver or kidney after 4 h from the therapy administration.

Discussion

In this study, we reported the design and validation of a platform for US and MB-mediated targeted delivery of FDA-approved PLGA-PEG NPs loaded with anticancer AmiR-21 and AmiR-10b in a large animal model. The objective of our work was to translate the drug delivery platform that we previously designed and tested in mice [12], as a further step toward clinical use. The platform was implemented on a commercially available scanner using a single curved array transducer for image-guided therapy and with clinical-grade MBs. We chose a pig model to test our system *in vivo* primarily because of anatomical similarities with humans, in particular with respect to the position and depth of liver and kidney, and due to our prior expertise with this animal model.

As a first step, we performed a phantom study to optimize the relevant acoustic parameters for maximizing ICD, as we aimed to determine if sufficient inertial cavitation of circulating MBs could be achieved at depth by using a diagnostic ultrasound transducer. We observed a plateau-like behavior for the measured ICD at higher pressures and pulse lengths. A possible explanation for this effect is that MBs were destroyed in a larger volume and to a greater extent while not being replenished quickly enough to increase the ICD. Similarly, the ICD decreased for increasing PRF, possibly due to the same effect. It is important to point out that the measured ICD is highly reliant on the specific setup used and cannot be generalized to different experimental situations. In addition, the phantom setup is not reflective of the vascular functioning *in vivo*, where MBs are replenished through a more complex vasculature. We used the results from the phantom study to inform the selection of acoustical parameters used for the *in vivo* experiments.

qRT-PCR quantification of delivered miRNAs showed a 1.9- and 2.7-fold increase in the liver and 3.7- and 2.8-fold increase in the kidney for exogenous AmiR-21 and AmiR-10b, respectively. These results are comparable to the amount of miRNA quantified in hepatocellular carcinoma xenografts in mice after US treatment [12]. miRNA levels were

overall higher in the liver due to clearance of the NPs in this organ. We show that at 24 h there is decreased exogenous AmiR-21 in the liver, kidney, and heart with respect to the level at 4 h, while the miRNA level increased substantially at 24 h in the lung and spleen. This may be due to the uptake of PLGA-PEG NPs by immune cells, which accumulate in these organs. Additionally, the accumulation of AmiR-21 in the lung may be the result of alveolar trapping of sticky phospholipids rather than intracellular uptake of PLGA-PEG NPs, as we did not observe accumulation of NPs in the lungs in previous studies where we systemically injected PLGA-PEG NPs without MBs in mice [3]. Hence, we are not concerned about the accumulation of AmiR-21 in the lung.

To confirm the presence of NPs in the liver parenchyma, we performed IF microscopy of fluorescent SPNs. The measured characteristics of the synthesized SPNs were similar to those of miRNA-loaded PLGA-PEG particles, therefore we expect these particles to behave similarly in terms of extravasation. Importantly, SPNs were not co-located with endothelial marker CD31, supporting the hypothesis of transvascular transport and entry of NPs in the extravascular compartment. Although we did not formally demonstrate in this study endocytosis of NPs by parenchymal cells, our previous studies have shown significantly higher intracellular miRNA level in cells treated with miRNA-loaded NPs compared to controls *in vitro* [3].

To the best of our knowledge, this is the first study demonstrating a platform for US-mediated delivery of miRNA-loaded PLGA-PEG NPs to deep tissues (70 mm) in large animals. Compared to previously reported studies [16], [18]–[20], here we decided to use PLGA-PEG particles as delivery vectors and facilitate NP extravasation through US/MB-mediated sonoporation rather than releasing naked drug directly from MBs or liposomes. This strategy offers the advantage of an increased miRNA circulation half-life to obtain a sustained and controlled release. Our findings in small animal models show presence of the injected miRNAs into the tumors for more than a week [3]. Hence, we envision a potentially effective therapeutic scheme involving treatment with miRNAs, possibly co-delivered with chemotherapeutic agents [21], on a weekly basis.

We acknowledge the presence of several limitations in our experimental design. First, a single animal was used for quantification of delivered miRNAs in the targeted regions, therefore we could not demonstrate reproducibility of the results. We performed the US/MB treatment on a total of four animals. Pigs 1, 2, and 3 received US therapy in the liver only and were euthanized 24 h post NP administration. We performed an US-guided injection of India ink immediately after the treatment to mark the targeted region and facilitate its identification *ex vivo*. However, we could not find traces of dye at necropsy and were unable to locate the targeted area in the liver, possibly due to the fast clearance of ink from the organ. We modified the experimental protocol in Pig 4 to euthanize at 4 h post NP administration. We kept the animal under anesthesia for the whole duration of the treatment to avoid significant organ displacement and injected a solution of Matrigel with ICG dye. The Matrigel solution solidifies immediately at 37 °C becoming a gelatinous matrix that is not quickly cleared by the liver. In the kidney, we t argeted the lower pole to facilitate localization based on the anatomy of the organ. The primary aim of this study was to determine if microbubble cavitation sufficient to enhance NP delivery could be achieved at

depth by using a diagnostic ultrasound transducer, as we move forward to use this platform for treatment of liver cancer in dogs. To this end, we demonstrated increased delivery of miRNA in the treated regions relative to control in deep tissues. Although we expect more variability with a larger number of animals in the amount of delivered microRNA, we expect this result to remain valid, as the delivered antisense miRNAs are not available in the animal system under normal conditions. Hence, the observed variations may not be attributable to other endogenous confounding factors. To mitigate the limitation of the low number of animals we have replicated the results in the liver and kidney in the same animal with two different antisense miRNAs.

A second limitation of our study was that only healthy animals were used, due to the challenges of producing a cancer model in pigs. Our future work will focus on delivering miRNA-loaded PLGA-PEG NPs in client-owned dogs with advanced liver cancer. While we expect increased levels of delivered miRNAs in cancer compared with healthy tissue due to the more fragile and leakier tumor vasculature, challenges may arise from hypovascularized or necrotic regions preventing circulating MBs and NPs to reach the target area.

Finally, our current implementation did not include measurement of cavitation signals during the administration of US therapy *in vivo*. Future implementations will include real-time cavitation monitoring to ensure optimal sonication conditions over the treatment period.

In conclusion, through this study we show the design and validation of a single-probe US platform for targeted delivery of miRNA-loaded PLGA-PEG NPs to deep organs in a pig model. The implemented platform represents a step further toward the translation of this targeted drug delivery system in humans.

Acknowledgements

This work is dedicated to the memory of Dr. Juergen K. Willmann, whose mind laid the foundations of this project. We thank Amy Thomas for assistance with the illustrations, Dr. Andrew Olson and the Stanford Neuroscience Microscopy Service for assistance with the confocal microscopy, and the Stanford Animal Histology Services for preparation of brightfield histology. This work was supported by the Focused Ultrasound Foundation and the National Institutes of Health (grants numbers R01CA209888 and R21EB022298). The Stanford Neuroscience Microscopy Service is supported by grant NIH NS069375.

Abbreviations

AmiRNA or AmiR	antisense-microRNA
ANOVA	analysis of variance
DLS	dynamic light scattering
DSPE-mPEG	1,2-Distearoyl-sn-glycero-3-phosphoethanolamine-N-[methoxy(polyethyleneglycol)-2000]
EPR	enhanced permeability and retention
FWHM	full width at half maximum
H&E	hematoxylin and eosin

ICD	inertial cavitation dose
ICG	indocyanine green
IF	immunofluorescence
MB	microbubble
MI	mechanical index
miRNA or miR	microRNA
NP	nanoparticle
NTA	nanoparticle tracking analysis
PDI	polydispersity index
PFODBT	poly[2,7-(9,9-dioctylfluorene)-alt-4,7-bis(thiophen-2-yl)benzothiadiazole]
PLGA-PEG	pegylated poly lactic-*co*-glycolic acid
PRF	pulse repetition frequency
qRT-PCR	quantitative reverse transcription polymerase chain reaction
RMS	root mean square
SPN	semiconducting polymer nanoparticle
US	ultrasound

References

[1]. Calin GA and Croce CM, “MicroRNA signatures in human cancers,” Nat. Rev. Cancer, vol. 6, pp. 857–866, 2006. [PubMed: 17060945]

[2]. Croce CM, “Causes and consequences of microRNA dysregulation in cancer,” Nat. Rev. Genet, vol. 10, pp. 704–714, 2009. [PubMed: 19763153]

[3]. Devulapally R et al., “Polymer Nanoparticles Mediated Codelivery of AntimiR-10b and AntimiR-21 for Achieving Triple Negative Breast Cancer Therapy,” ACS Nano, vol. 9, no. 3, pp. 2290–2302, 2015. [PubMed: 25652012]

[4]. Chowdhury SM et al., “Ultrasound-guided therapeutic modulation of hepatocellular carcinoma using complementary microRNAs,” J. Control. Release, vol. 238, pp. 272–280, 2016. [PubMed: 27503707]

[5]. Mitchell PS et al., “Circulating microRNAs as stable blood-based markers for cancer detection,” Proc. Natl. Acad. Sci. U.S.A, vol. 105, no. 30, pp. 10513–10518, 2008. [PubMed: 18663219]

[6]. V Pecot C, Calin GA, Coleman RL, Lopez-Berestein G, and Sood AK, “RNA interference in the clinic: challenges and future directions,” Nat. Rev. Cancer, vol. 11, pp. 59–67, 2011. [PubMed: 21160526]

[7]. Jain RK and Stylianopoulos T, “Delivering nanomedicine to solid tumors,” Nat. Rev. Clin. Oncol, vol. 7, no. 11, pp. 653–664, 2010. [PubMed: 20838415]

[8]. Allen TM and Cullis PR, “Drug Delivery Systems: Entering the Mainstream,” Science (80-.)., vol. 303, pp. 1818–1822, 2004.

[9]. Bae YH and Park K, “Targeted drug delivery to tumors: Myths, reality and possibility,” J. Control. Release, vol. 153, no. 3, pp. 198–205, 2011. [PubMed: 21663778]

[10]. Ferrara K, Pollard R, and and Borden Mark, “Ultrasound Microbubble Contrast Agents: Fundamentals and Application to Gene and Drug Delivery,” Annu. Rev. Biomed. Eng, vol. 9, pp. 415–47, 2007. [PubMed: 17651012]

[11]. Hernot S and Klibanov AL, “Microbubbles in ultrasound-triggered drug and gene delivery,” Adv. Drug Deliv. Rev, vol. 60, pp. 1153–1166, 2008. [PubMed: 18486268]

[12]. Wang T-Yet al., “Ultrasound-guided delivery of microRNA loaded nanoparticles into cancer,” J. Control. Release, vol. 203, pp. 99–108, 2015. [PubMed: 25687306]

[13]. Kotopoulis S et al., “Sonoporation-Enhanced Chemotherapy Significantly Reduces Primary Tumour Burden in an Orthotopic Pancreatic Cancer Xenograft,” Mol. Imaging Biol, vol. 16, pp. 53–62, 2014. [PubMed: 23877869]

[14]. Nesbitt H et al., “Gemcitabine loaded microbubbles for targeted chemo-sonodynamic therapy of pancreatic cancer,” J. Control. Release, vol. 279, pp. 8–16, 2018. [PubMed: 29653222]

[15]. Kinoshita M, McDannold N, Jolesz FA, and Hynynen K, “Noninvasive localized delivery of Herceptin to the mouse brain by MRI-guided focused ultrasound-induced blood-brain barrier disruption,” Proceedings, vol. 103, no. 31, pp. 11719–11723, 2006.

[16]. Dimcevski G et al., “A human clinical trial using ultrasound and microbubbles to enhance gemcitabine treatment of inoperable pancreatic cancer,” J. Control. Release, vol. 243, pp. 172–181, 2016. [PubMed: 27744037]

[17]. Lipsman N et al., “Blood-brain barrier opening in Alzheimer’s disease using MR-guided focused ultrasound,” Nat. Commun, vol. 9, p. 2336, 2018. [PubMed: 30046032]

[18]. Dewitte H et al., “Theranostic mRNA-loaded Microbubbles in the Lymphatics of Dogs: Implications for Drug Delivery,” Theranostics, vol. 5, no. 1, pp. 97–109, 2015. [PubMed: 25553101]

[19]. Liu Y, Li L, Su Q, Liu T, Ma Z, and Yang H, “Ultrasound-targeted microbubble destruction enhances gene expression of microRNA-21 in swine heart via intracoronary delivery,” Echocardiography, vol. 32, pp. 1407–1416, 2015. [PubMed: 25613289]

[20]. Lyon PC et al., “Safety and feasibility of ultrasound-triggered targeted drug delivery of doxorubicin from thermosensitive liposomes in liver tumours (TARDOX): a single-centre, open-label, phase 1 trial,” Lancet Oncol., vol. 19, no. 8, pp. 1027–1039, 2018. [PubMed: 30001990]

[21]. Chowdhury SM et al., “Longitudinal assessment of ultrasound-guided complementary microRNA therapy of hepatocellular carcinoma,” J. Control. Release, vol. 281, pp. 19–28, 2018. [PubMed: 29758233]

[22]. Devulapally R and Paulmurugan R, “Polymer nanoparticles for drug and small silencing RNA delivery to treat cancers of different phenotypes,” Wiley Interdiscip. Rev. Nanomed. Nanobiotechnol, vol. 6, pp. 40–60, 2013. [PubMed: 23996830]

[23]. Garzon R, Calin GA, and Croce CM, “MicroRNAs in Cancer,” Annu. Rev. Med, vol. 60, pp. 167–79, 2009. [PubMed: 19630570]

[24]. Karaman M, Li PC, and O’Donnell M, “Synthetic Aperture Imaging for Small Scale Systems,” IEEE Trans. Ultrason. Ferroelec., Freq. Contr, vol. 42, no. 3, pp. 429–442, 1995.

[25]. Jensen JA, Nikolov S, Gammelmark KL, and Pedersen MH, “Synthetic aperture ultrasound imaging,” Ultrasonics, vol. 44, pp. e5–e15, 2006. [PubMed: 16959281]

[26]. “LUMASON (sulfur hexafluoride lipid-type A microspheres) for injectable suspension, for intravenous use or intravesical use,” 2016 [Online]. Available: https://www.accessdata.fda.gov/drugsatfda_docs/label/2016/203684s002lbl.pdf.

[27]. Chen W-S, Brayman AA, Matula TJ, and Crum LA, “Inertial Cavitation Dose and Hemolysis Produced In Vitro with or without Optison,” Ultrasound Med. Biol, vol. 29, no. 5, pp. 725–737, 2003. [PubMed: 12754072]

[28]. Maxwell AD, Cain CA, Hall TL, Fowlkes JB, and Xu Z, “Probability of Cavitation for Single Ultrasound Pulses Applied to Tissues and Tissue-Mimicking Materials,” Ultrasound Med. Biol, vol. 39, no. 3, pp. 449–465, 2013. [PubMed: 23380152]

[29]. Pu K et al., “Semiconducting polymer nanoparticles as photoacoustic molecular imaging probes in living mice,” Nat. Nanotechnol, vol. 9, pp. 233–239, 2014. [PubMed: 24463363]

[30]. Livak KJ and Schmittgen TD, “Analysis of Relative Gene Expression Data Using Real-Time Quantitative PCR and the 2-ΔΔCT Method,” Methods, vol. 25, no. 4, pp. 402–408, 12 2001. [PubMed: 11846609]

[31]. Schindelin J et al., “Fiji: an open-source platform for biological-image analysis,” Nat. Methods, vol. 9, pp. 676–682, 2012. [PubMed: 22743772]

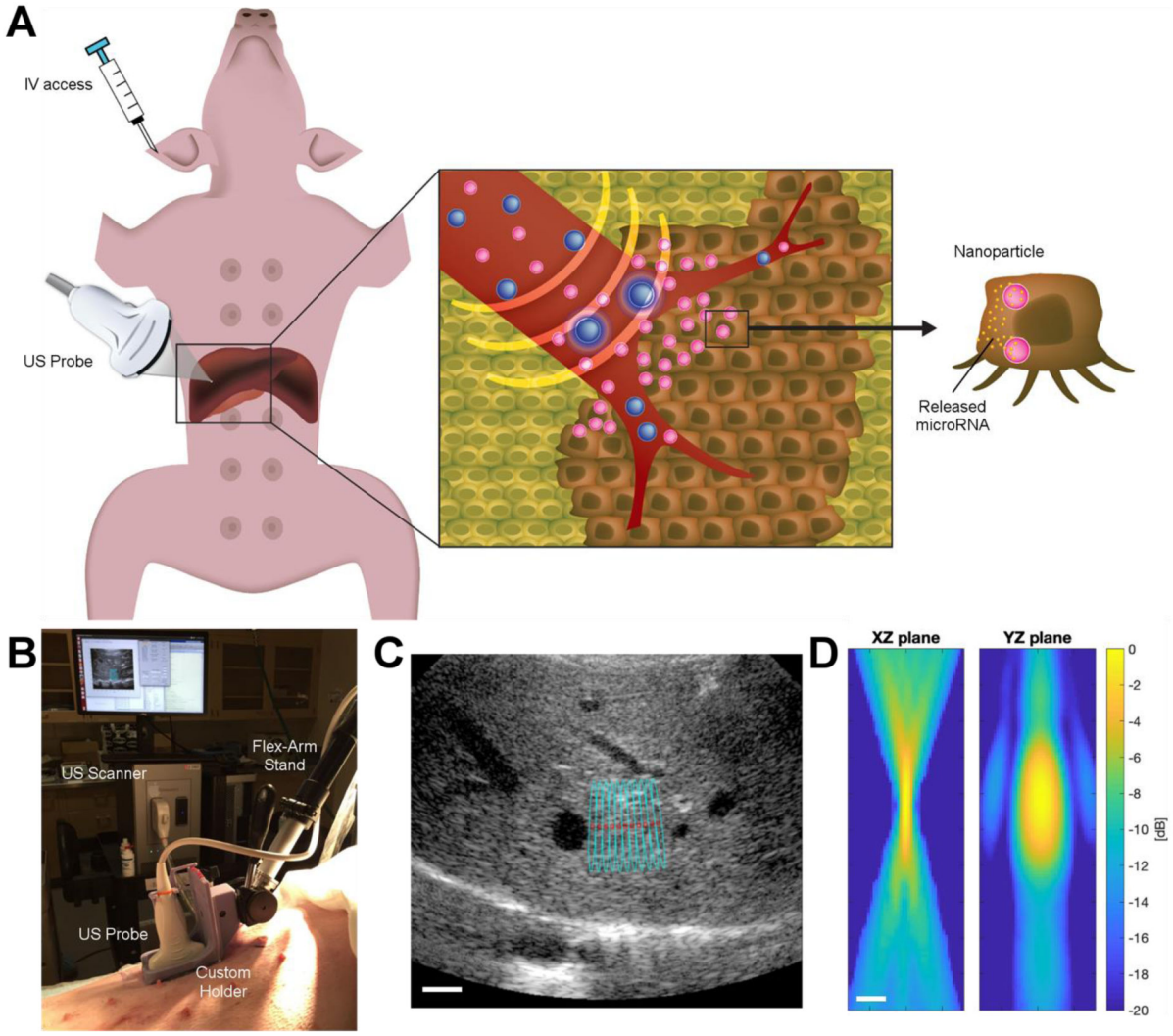

Figure 1.

(**A**) Schematic representation of the ultrasound-mediated drug delivery platform. MBs (blue) and NPs (pink) are co-administered intravenously and circulate in the blood pool (red). MBs cavitating under the effect of a focused US beam increase the vascular permeability facilitating NP extravasation. The NPs then release their miRNA cargo. (**B**) Picture of the setup during an animal experiment. The image shows the US probe mounted on the flex-arm stand. (**C**) B-mode image of the pig liver used for therapy guidance. The US therapy focal regions are overlaid and depicted in cyan. (**D**) Hydrophone measurements of the focused US beam in the lateral (XZ) and elevation (YZ) planes. Scale bar: 1 cm in (**C**); 2 mm in (**D**).

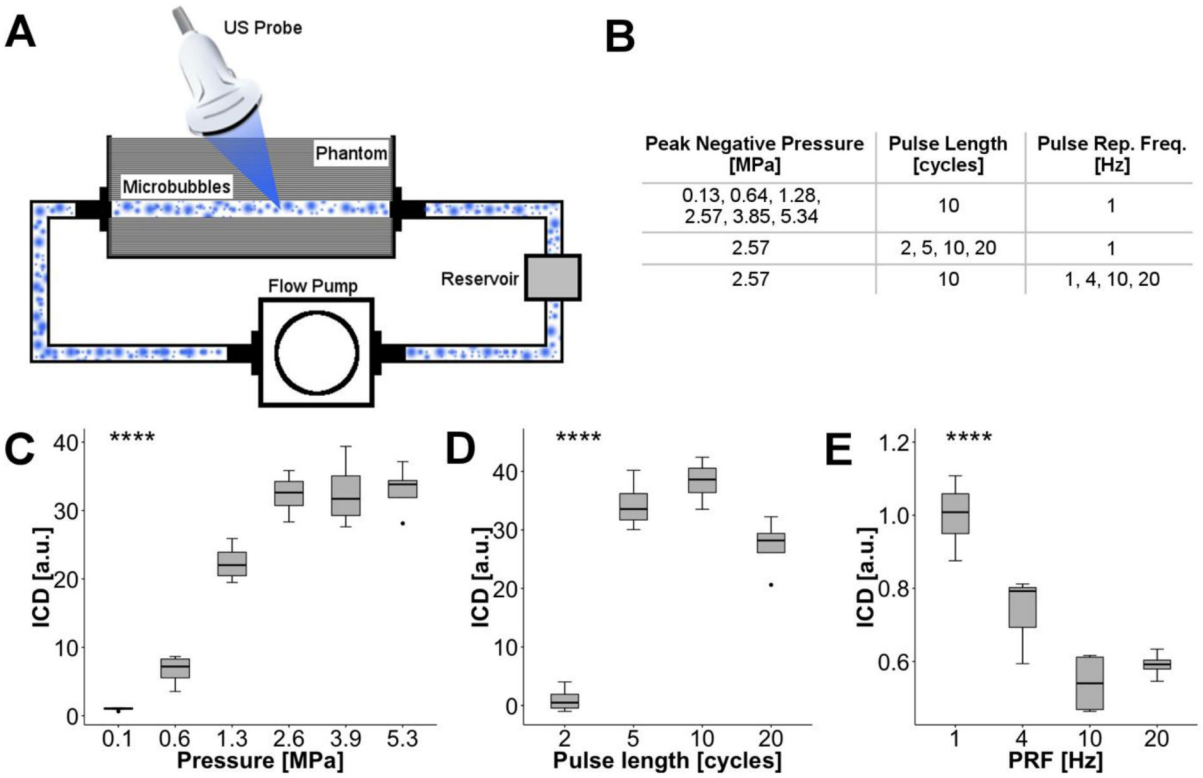

Peak Negative Pressure [MPa]	Pulse Length [cycles]	Pulse Rep. Freq. [Hz]
0.13, 0.64, 1.28, 2.57, 3.85, 5.34	10	1
2.57	2, 5, 10, 20	1
2.57	10	1, 4, 10, 20

Figure 2.

(**A**) Schematic representation of the phantom setup used for assessing the effect of varying acoustic parameters on the measured ICD. (**B**) Parameters tested in the phantom study. (**C, D, E**) Box plots showing the effect of peak negative pressure, pulse length, and pulse repetition frequency on the measured ICD. In each box plot, the rectangle spans the interquartile range, the bar inside the rectangle represents the median, and the whiskers show the minimum and maximum values. The ICD was significantly influenced by all the tested parameters. Results of ANOVA are shown in the upper-left corner of each plot (n = 4; ****: $p < 0.0001$). A plateau-like behavior was observed, with no statistical difference between pressures of 2.57, 3.85, and 5.34 MPa, pulse lengths of 5, 10, and 20 cycles, and pulse repetition frequency (PRF) of 4, 10, and 20 Hz.

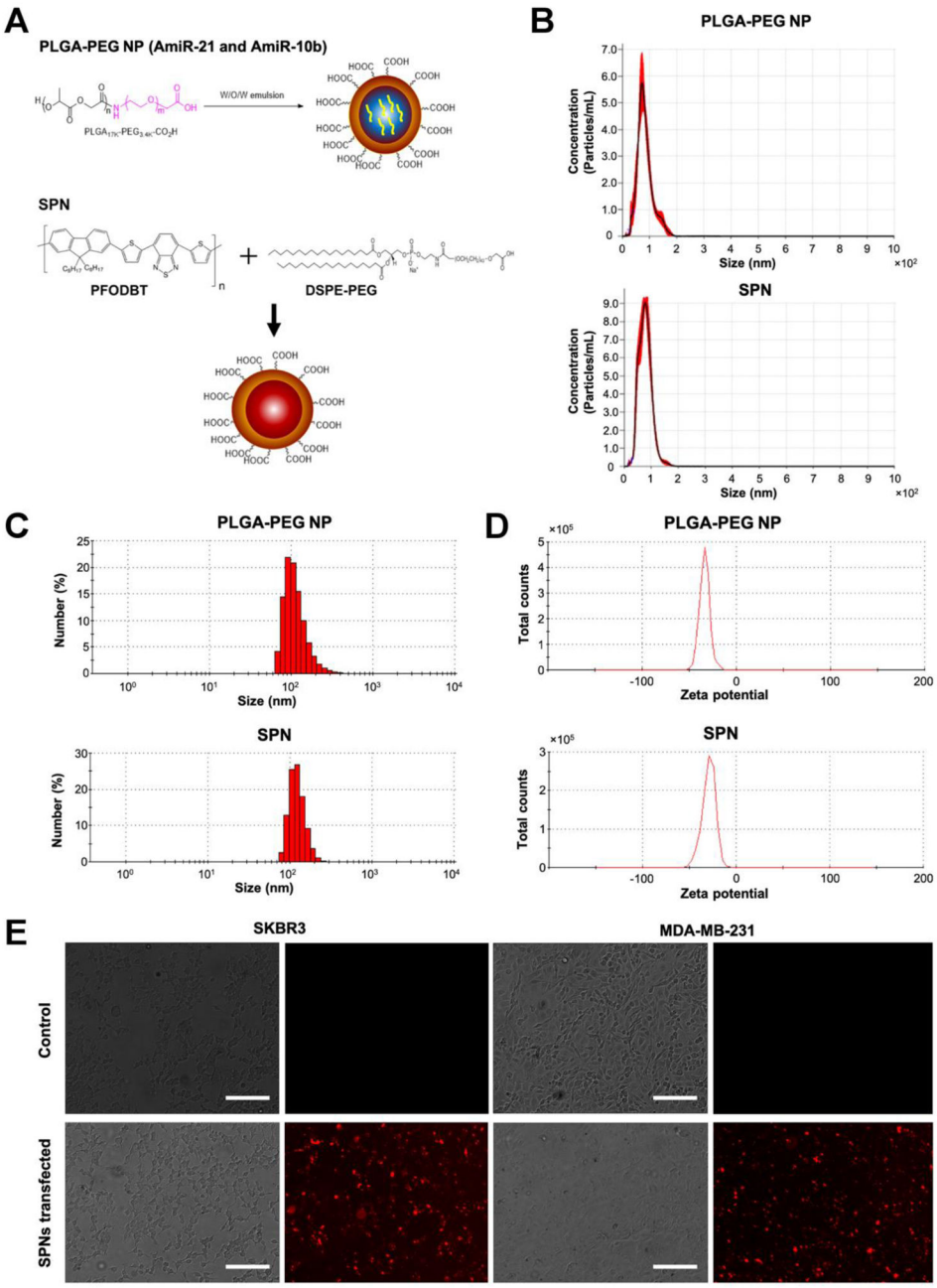

Figure 3.

Nanoparticle preparation and characterization. (**A**) Schematic illustration of PLGA-PEG NPs (top) and SPNs (bottom). (**B**) Particle concentration quantified through nanoparticle tracking analysis (NTA). (**C, D**) Particle size distribution and zeta-potential quantified by dynamic light scattering (DLS) analysis. (**E**) Brightfield (left) and confocal fluorescent microscope (right) images of SKBR3 and MDA-MB-231 cell lines with (bottom) and without (top) incubation with SPNs. Scale bar: 100 μm.

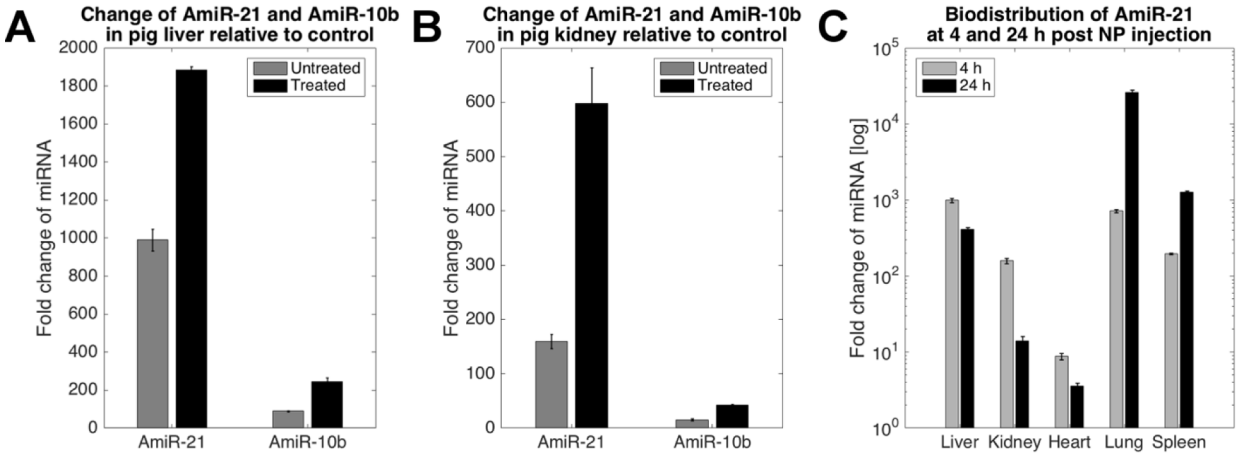

Figure 4.

qRT-PCR quantification of exogenously delivered AmiR-21 and AmiR-10b in Pigs 3 and 4. The miRNA levels are expressed as fold changes relative to expression of miR-122 in the liver and kidney of a negative control animal (Pig 5) that was administered neither drug-loaded PLGA-PEG NPs nor US and MB therapy. The vertical bars in each plot report the mean of three qRT-PCR quantifications and the whiskers show ±1 time the standard deviation. (**A**) Levels of AmiR-21 and AmiR-10b in the liver of Pig 4 in an untreated region and in the area treated with US and MB therapy. (**B**) Levels of AmiR-21 and AmiR-10b in the kidney of Pig 4 in the untreated region and in the area treated with US and MB therapy. (**C**) Biodistribution of AmiR-21 at 4 h (Pig 4) and 24 h (Pig 3) after injection of miRNA-loaded PLGA-PEG NPs.

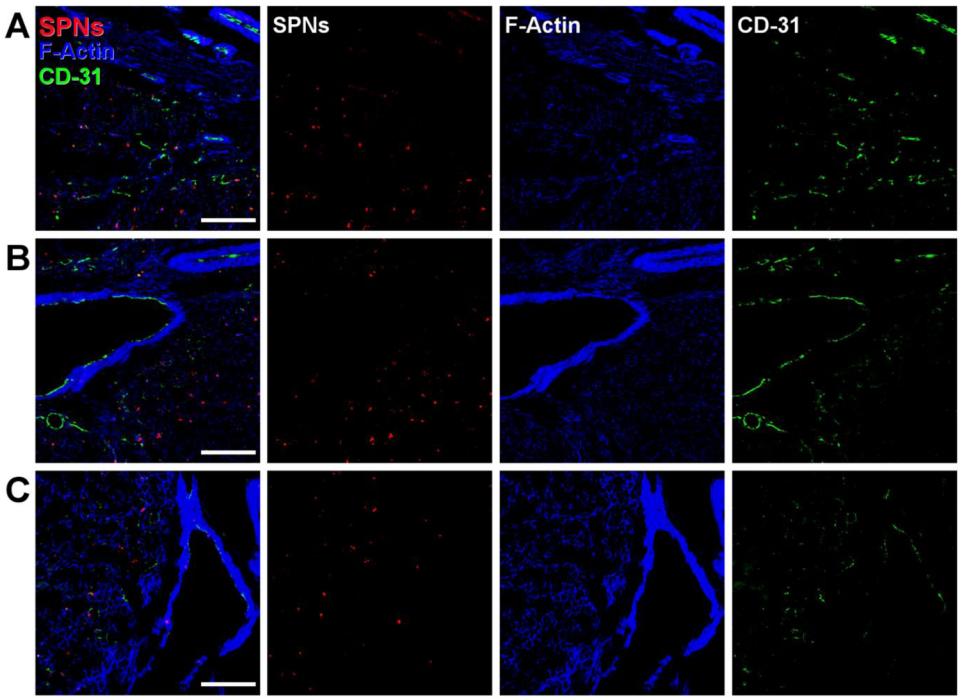

Figure 5.

Representative immunofluorescence images of SPNs (red) in pig liver (Pig 4). The samples were stained for endothelial cell marker CD-31 (green) and F-actin (blue) for the visualization of blood vessels and cytoskeleton, respectively. (**A** and **B**) Merged and split channels in two different sections sampled in the treated volume. (**C**) Merged and split channels of a section in an untreated region. Scale bar: 100 μm.

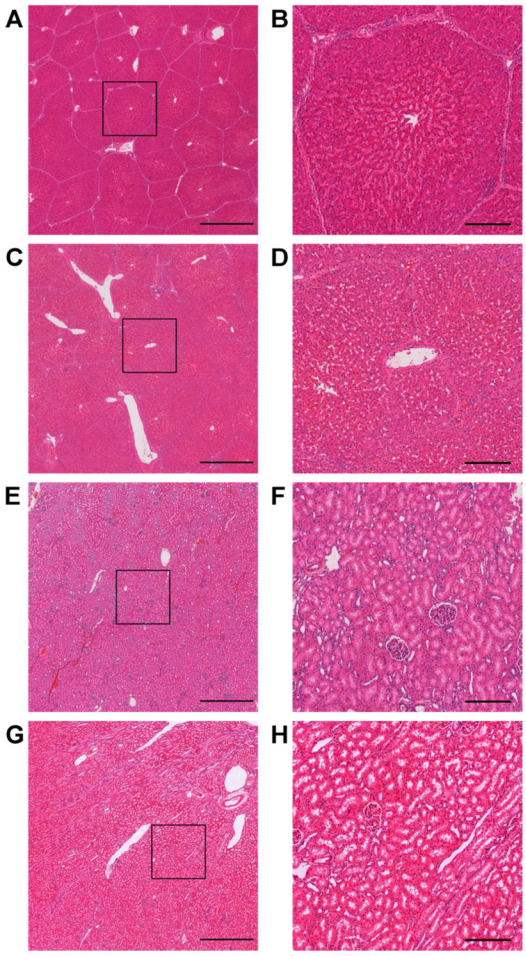

Figure 6.

Representative H&E images of pig tissue (Pig 4). Liver samples for treated and untreated regions are shown in (**A**) and (**C**), respectively. Kidney samples for treated and untreated regions are shown in (**E**) and (**G**), respectively. (**B**), (**D**), (**F**), and (**H**) show magnification of the areas inside the black square in (**A**), (**C**), (**E**), and (**G**), respectively. Scale bar: 1 mm in (**A**), (**C**), (**E**), (**G**); 200 μm in (**B**), (**D**), (**F**), (**H**).